Motion Planning by Demonstration With Human-Likeness Evaluation for Dual-Arm Robots

Néstor García⬚, Jan Rosell, and Raúl Suárez, *Member, IEEE*

Abstract—This paper presents a planning procedure that allows an anthropomorphic dual-arm robotic system to perform a manipulation task in a natural human-like way by using demonstrated human movements. The key idea of the proposal is to convert the demonstrated trajectories into attractive potential fields defined over the configuration space and then use an RRT*-based planning algorithm that minimizes a path-cost function designed to bias the tree growth toward the human-demonstrated configurations. This paper presents a description of the proposed approach as well as results from a conceptual and a real application example, the latter using a real anthropomorphic dual-arm robotic system. A path-quality measure, based on first-order synergies (correlations between joint velocities) obtained from real human movements, is also proposed and used for evaluation and comparison purposes. The obtained results show that the paths obtained with the proposed procedure are more human-like.

Index Terms—Human-like motions, humanoid robots, path planning for manipulators, synergies.

I. INTRODUCTION

MOTION planning is a basic research issue in robotics, particularly since the robots became an essential part in many application fields like, for instance, the medical and the electronic industries, or even in the computational biology or computer animation fields. The importance of this problem is more relevant for robotic systems with a high number of degrees of freedom (DOFs), like those involving mechanical hands or anthropomorphic structures. Moreover, a path is sometimes required that, besides being collision-free, also optimizes a quality measure like minimizing the traveled distance [1] or the time required in the path execution [2]. In the case of humanoid robots, one of the needs is to find robot movements that mimic those of human beings, since human-robot collaboration is facilitated if the robot shows human-like movements [3] because when humans are familiar with the robot motions, they may adjust their motions to avoid possible collisions or enhance the collaboration.

Different planning algorithms able to tackle the motion planning of complex systems have been developed, being the sampling-based planners the most outstanding [4]. Among them, the most commonly used are the probabilistic roadmaps (PRMs) [5] and the rapidly exploring random trees (RRTs) [6]. Diverse improvements have been proposed to these planners to deal with constraints [7], to consider configuration-space costmaps [8], or to bias the sampling toward better regions of the configuration space by using, for instance, retraction-based methods [9] or principal component analysis (PCA) [10]. Since these algorithms are nonoptimal, other variants like the PRM* and RRT* algorithms have been proposed [11]. Besides, recently, the RRT* planner was combined with potential fields in order to improve its efficiency [12] and guide the solution path [13]. In this line, this paper proposes the use of a variant of the RRT* algorithm that minimizes a path-cost function computed with a potential field obtained from human demonstrations, thus resulting in human-like motions. Potential functions learned from human demonstrations have been also used in control policies [14].

Looking for human-like movements leads to the search of the right coordination between the robot joint movements. Toward this goal, the direct use of the real movements of a human being as a reference is common [15]. On the one hand, a usual assumption of many approaches analyzing human motion is that humans try to minimize an unknown cost function while doing everyday manipulation tasks, e.g., hand jerk (i.e., the third time-derivative of the hand position) [16], joint jerk [17], joint torque [18], or a convex combination of several cost functions with weighting factors chosen to describe an observed human motion [19]. Hence, minimizing these cost functions, human-like motions can be obtained. However, it can be complex to incorporate these functions in the inverse kinematics of some manipulators. On the other hand, new human-like movements can be obtained using human motions previously registered, e.g., by properly modifying these motions to fit a new scenario [20], by using these known movement trajectories to train a neural network [21] or to adjust the parameters of a nonlinear dynamical system [22]. Other related advanced procedures include, e.g., the generation of cyclic motions for dual-arm robots using neural networks and quadratic programming [23], the consideration of the robot

dynamics in the motion planning by transforming the problem into an optimization of a nonlinear fitness function [24] or the use of movement primitives based on a model of the triangle defined by the human upperarm and forearm [25].

In the motion planning of mechanical hands, several works used "postural synergies" (i.e., correlations between DOFs) to simplify the problem by reducing the dimension of the search space as well as to mimic human postures. The correlations of the human hand configurations while performing a grasp were studied [26] and mapped into a robotic hand [27]. These synergies were suggested to be an emergent consequence of neuromuscular impedance [28]. The synergies existing in the human hand [29] were also used for other objectives such as the analysis and design of robotic hands in order to mimic human grasps [30], the selection of grasping forces [31], and the design of specific hand control systems [32]. Later, a compliant model for synergies, called "soft synergies," was introduced and used in the selection of grasping forces, in their control, and in the control of the motion of the grasped object [31], [33]. The use of synergies was recently also used in a dual-arm anthropomorphic system while performing manipulation tasks [34], [35]. One of the main problems faced when trying to obtain human synergies is the capture of the human configurations in order to get proper information for the search of the synergies. In the case of the hands mentioned above, the problem was mainly addressed using: 1) vision systems (e.g., [36]) which have the frequent problem of visual occlusions and usually require special marks on the hand to facilitate the configuration identification and 2) sensorized gloves (e.g., [37]). In the particular application of moving a prosthetic hand, the analysis of forearm electromyogram signals was proposed (e.g., [38]) but this is not practical in most general-purpose robotic applications.

The works mentioned above dealt with synergies involving correlations between joint positions. Nevertheless, a recent work extends the concept of synergies to the velocity space (i.e., the space of the first derivative of the configuration trajectories) calling them first-order synergies [39], [40] (in contrast with the synergies in the configuration space, that were called zero-order synergies). In this line, this paper proposes a human-likeness index based on first-order synergies and uses it to evaluate the paths obtained with the proposed motion planner based on human demonstrations.

After this introduction, Section II presents the problem statement and the approach overview, and Section III outlines the required preliminaries. Then, Section IV details the proposal of the planner and its performance analysis, and Section V introduces the human-likeness index and uses it to evaluate the proposed planner. Finally, Section VI presents the conclusion and future work.

II. MOTIVATION AND APPROACH OVERVIEW

The first goal of this paper is to introduce a planning procedure designed specifically for anthropomorphic dual-arm robotic systems that solves manipulation tasks using human-like paths. To this end, the movements of a human operator are used as demonstration paths. The main features of the proposed approach are as follows (see Fig. 1).

1) The movements of a human operator solving manipulation tasks are captured and then mapped to the anthropomorphic dual-arm robotic system.
2) The demonstration paths are used to generate attractive potential fields over the configuration space $\mathcal{C}$.
3) The captured movements are also used to select a region of a lower-dimensional subspace of $\mathcal{C}$, called B_k, that contains a predefined high percentage of the sample variance of the demonstration paths. By planning in this subspace, a significant reduction of the computational cost is expected.
4) Using the potential fields generated in $\mathcal{C}$, a path cost is defined to guide an RRT*-based planner. The proposed planning algorithm uses a stochastic gradient-descent method to minimize the path cost and to bias the tree growth toward the demonstrated human movements.

The second goal of this paper is to define a quality index to evaluate the human-likeness of a path by considering how much aligned the path is with respect to certain reference human movements. These movements, which can be different to the ones used as demonstration paths to solve the task, are characterized by using a set of first-order synergies defined over the relevant configurations of $\mathcal{C}$.

Note that, since the two goals are clearly independent, they are addressed separately in Sections IV and V, respectively, each one with its own experimentation. Thereby, first a path is obtained with the proposed planner using demonstrations (Section IV), and then the human-likeness of the planned path is evaluated (Section V); this human-likeness index can be used to evaluate the paths obtained with the proposed planning procedure or with any other motion planner.

III. PRELIMINARIES

This section presents some basic concepts and procedures (introduced in previous works [13], [34], [39]) that are relevant to the present proposal.

A. Capturing and Mapping Human Motions

Human movements are used to guide the motion planning to find human-like paths for dual-arm systems and to evaluate the human-likeness of the paths. Human motions can be captured and mapped to the robot configuration space in different ways, depending on the available sensors and on the robot kinematics. In this paper, magnetic trackers and sensorized gloves are used to take samples of the position and orientation of the operator wrists while performing manipulation tasks [see Fig. 1(top-left)]. Then, the captured data are mapped to the dual-arm robotic system by solving the inverse kinematics of the arms for each sampled wrist configuration, obtaining in this way the corresponding configurations of the dual-arm system. Inverse kinematics of robotic arms usually have several solutions, or even infinite in the case of redundant arms with more than 6 DOFs, therefore some anthropomorphism criterion should be used to solve it (e.g., controlling the position of the robot elbows [41]).

In this way, for each task execution done by the operator, a sequence of configuration samples is obtained in the robot
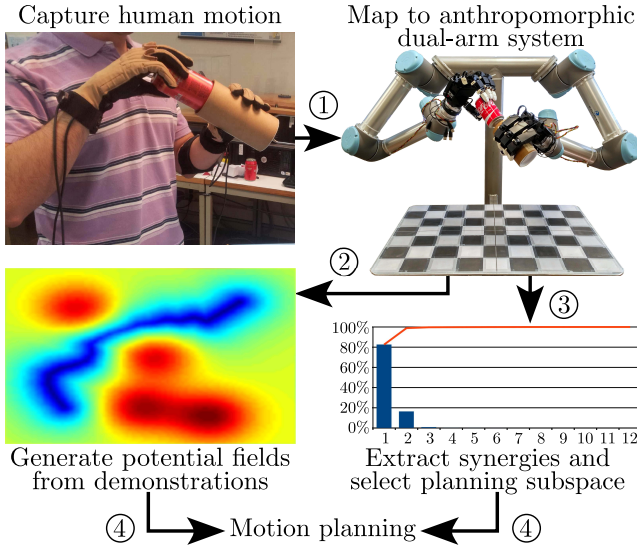
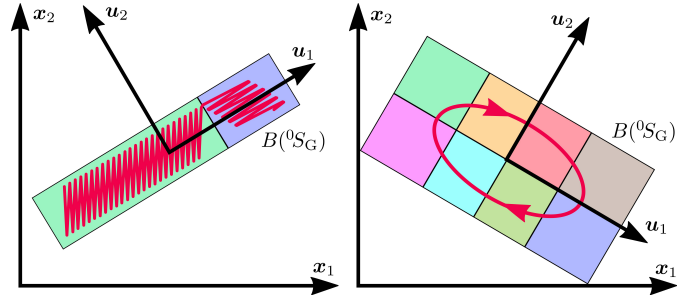Fig. 1.   General schema of the proposed approach.

Fig. 2.   Ray-shaped motion (left) and an elliptic motion (right), shown in red, with the resulting cell-decomposition of $\mathcal{C}$ based on the first-order synergy differences. Boxes $B(^0S_G)$ have been split into two and eight cells, respectively, with planes aligned with the ^0S_G axes (i.e., u_1 and u_2).

configuration space $\mathcal{C}$, defining a sequence $\mathcal{P}_i$ of rectilinear segments connecting time-consecutive mapped configurations. In our case, the dual-arm system used is composed of two UR5 6-DOF robotic arms from Universal Robots, assembled emulating the human arm configuration as shown in Fig. 1(top-right), each arm being equipped with a 16-DOF Allegro Hand from Simlab (although this paper is only focused in the motions of the arms).

B. Zero- and First-Order Synergies

The postural synergies are correlations between the joint positions of an articulated system [30]. This widely used concept was called zero-order synergies in [39], where the extension to the joint velocity space was proposed, introducing the concept of first-order synergies as correlations between joint velocities. The zero-order synergies are obtained from the PCA of a set of captured configuration samples. This returns a new basis of $\mathcal{C}$, called zero-order basis ^0S, with the axes ordered according to the sample dispersions along them. Each axis represents a zero-order synergy and the movement along it, equivalent to a single DOF, implies the correlated movement of several (or all) the actual DOFs of the system. The procedure to obtain the first-order synergies is exactly the same as the one to obtain zero-order synergies, but in this case using velocity samples. Thereby, the new bases of the velocity space, defined by a barycenter μ and a covariance matrix Σ of velocity samples, are called first-order bases, ^1S, and each axis of the bases ^1S represents a first-order synergy.

The linear approximation of the PCA is enough to represent the subspace where the demonstrated motions lie. In fact, it has been demonstrated to be useful and implementable by a drive mechanism [42] or a real-time algorithm [43]. However, nonlinear approaches to obtain synergies have been also proposed, such as the Gaussian process latent variable model [26] and the unsupervised kernel regression [44].

The zero-order synergies are used to detect the relevant region of $\mathcal{C}$, called box $B(^0S_G)$, where the captured motions take place. Notice that the directions of the human motions

depend on the region of the configuration space where it takes place. Therefore, to take this into account, the box $B(^0S_G)$ is divided into subregions where the ^1S bases are significantly different, as introduced in [39]. As an example, Fig. 2 shows the box $B(^0S_G)$ and its resulting partition based on differences of first-order synergies for the samples of a motion that follows a ray shape and for the samples of another motion that follows an elliptic trajectory in clock-wise sense. For the ray-shaped motion, $B(^0S_G)$ is split into two parts, where the motion directions differ significantly from each other; and for the elliptic motion, $B(^0S_G)$ is split into eight cells.

Note that first-order synergies always exist if the sampled joint values are not homogeneously distributed, which is quite unlike in real human movements (that is why the first-order synergies are useful in the analysis of human movements).

In this paper:
1) the ^0S basis is used to define the lower-dimensional subspace where the planning will be done (Section IV);
2) the ^1S bases are used to define a human-likeness index to evaluate the solution paths found for the dual-arm robotic systems (Section V).

C. Motion-Cost Function

An RRT*-based planner recently proposed allows the user to guide the tree growth in a simple and transparent way [13]; this is done by defining attractive and repulsive points and segments in the workspace that generate a potential field $V(q)$ in the configuration space $\mathcal{C}$. Then, the planner constructs low-cost paths following the resulting valleys and saddle points in $\mathcal{C}$. Considering piece-wise linear paths in $\mathcal{C}$, the path cost is computed by adding the costs of the rectilinear segments (called motions). The cost of a motion between two configurations q_i and q_f is defined as the linear combination of three other costs c_P, c_I, and c_D with respective positive weights ω_P, ω_I and ω_D

$$c(q_i, q_f) = \omega_P \underbrace{\|q_f - q_i\|}_{c_P(q_i, q_f)} + \omega_I \underbrace{\int_{q_i}^{q_f} V(q)\, dq}_{c_I(q_i, q_f)}$$
$$+ \omega_D \underbrace{\int_{q_i}^{q_f} \left| \frac{\partial V(q)}{\partial q} \right| dq}_{c_D(q_i, q_f)} \qquad (1)$$

where c_P calculates the motion length, c_I measures the motion effort, computed as the product of the average value of $V(\boldsymbol{q})$ and the motion length, and c_D evaluates the variations of $V(\boldsymbol{q})$ along the motion. Therefore, the path minimizing this motion-cost function connects the start and the goal configurations in the shortest way that avoids the areas with high $V(\boldsymbol{q})$ values (i.e., with repulsive potential fields) and, at the same time, keeps $V(\boldsymbol{q})$ as monotonic as possible along the path (i.e., avoiding unneeded motions from repulsive to attractive potential fields and vice versa).

In this paper, the potential field is generated using real human movements and the motion-cost function guides the solution path toward these demonstrated human motions.

IV. PROPOSED MOTION PLANNING PROCEDURE

A. Generating Potential Fields From Demonstrations

The proposed planning algorithm tries to follow the demonstrated human movements by minimizing the cost of the path over the configuration space $\mathcal{C}$, where several potential fields are defined to guide the tree growth. For this, the demonstration paths generate attractive potential fields. In addition, the goal configuration $\boldsymbol{q}_{goal}$ acts also as an attractor. On the other hand, the obstacles generate potential fields that repulse the robotic arms while the arms also repel each other. To compute the potential-field value $V(\boldsymbol{q})$, let first:

1) $\lambda \geq 0$ and $\sigma \geq 0$ be, respectively, the strength and the diffusion parameters of each potential field;
2) $\mathcal{P}_i \in P$ be the ith path of the set of demonstration paths P, obtained from the mapping of the human movements and projected onto $\mathcal{C}$;
3) $\mathcal{O}_j \in O$ be the jth obstacle of the set of obstacles O with which the dual-arm system can collide;
4) $d(\boldsymbol{q}, \mathcal{P}_i)$ be the minimum distance in $\mathcal{C}$, between the configuration $\boldsymbol{q}$ and the demonstration path $\mathcal{P}_i$;
5) $d(\mathcal{L}_{\boldsymbol{q}}, \mathcal{R}_{\boldsymbol{q}})$ be the minimum distance in the workspace between both arms of the robotic system, when the dual-arm robot configuration is $\boldsymbol{q}$;
6) $d(\mathcal{L}_{\boldsymbol{q}}, \mathcal{O}_j)$ and $d(\mathcal{R}_{\boldsymbol{q}}, \mathcal{O}_j)$ be the minimum distances in the workspace between the obstacle $\mathcal{O}_j$ and the left arm and the right arm, respectively, when the dual-arm robot configuration is $\boldsymbol{q}$.

Then, the resultant potential-field value $V(\boldsymbol{q})$ at a collision-free configuration $\boldsymbol{q}$ is defined as the sum of four potential fields values

$$V(\boldsymbol{q}) = V_{\text{goal}}(\boldsymbol{q}) + V_{\text{paths}}(\boldsymbol{q}) + V_{\text{arms}}(\boldsymbol{q}) + V_{\text{obs}}(\boldsymbol{q}) \quad (2)$$

where

$$V_{\text{goal}}(\boldsymbol{q}) = \lambda_{\text{goal}}\left(1 - e^{-\sigma_{\text{goal}}\|\boldsymbol{q} - \boldsymbol{q}_{goal}\|^2}\right) \quad (3)$$

is the potential-field value of the configuration $\boldsymbol{q}$ regarding the attractive potential field of the goal configuration $\boldsymbol{q}_{goal}$ (i.e., the closer are $\boldsymbol{q}$ and $\boldsymbol{q}_{goal}$ and the smaller is V_{goal})

$$V_{\text{paths}}(\boldsymbol{q}) = \sum_{i}^{|P|} \frac{\lambda_i}{|P|}\left(1 - e^{-\sigma_i d(\boldsymbol{q}, \mathcal{P}_i)^2}\right) \quad (4)$$

is the potential-field value of the configuration $\boldsymbol{q}$ regarding the attractive potential fields generated by all the demonstration

paths $\mathcal{P}_i \in P$, i.e., V_{paths} decreases when $\boldsymbol{q}$ gets closer to P [it must be noted that, since $\mathcal{P}_i$ and $\boldsymbol{q}$ are both expressed in $\mathcal{C}$, $d(\boldsymbol{q}, \mathcal{P}_i)$ is simply the minimum Euclidean distance in $\mathcal{C}$ between $\boldsymbol{q}$ and the rectilinear segments representing $\mathcal{P}_i$]

$$V_{\text{arms}}(\boldsymbol{q}) = \lambda_{\text{arms}} e^{-\sigma_{\text{arms}} d(\mathcal{L}_{\boldsymbol{q}}, \mathcal{R}_{\boldsymbol{q}})^2} \quad (5)$$

is the potential-field value of the configuration $\boldsymbol{q}$ regarding the repulsive potential field between the arms of the robotic system, i.e., V_{arms} grows if the arms get closer; and

$$V_{\text{obs}}(\boldsymbol{q}) = \sum_{j=1}^{|O|} \frac{\lambda_j}{|O|}\left(e^{-\sigma_j d(\mathcal{L}_{\boldsymbol{q}}, \mathcal{O}_j)^2} + e^{-\sigma_j d(\mathcal{R}_{\boldsymbol{q}}, \mathcal{O}_j)^2}\right) \quad (6)$$

is the potential-field value of the configuration $\boldsymbol{q}$ regarding the repulsive potential fields of all the obstacles $\mathcal{O}_j \in O$, if either the left arm or the right arm of the robotic system gets close to any $\mathcal{O}_j$, then V_{obs} increases.

To speed up the computation of $V(\boldsymbol{q})$, the distances between the robotic arms and the obstacles [i.e., $d(\mathcal{L}_{\boldsymbol{q}}, \mathcal{R}_{\boldsymbol{q}})$, $d(\mathcal{L}_{\boldsymbol{q}}, \mathcal{O}_j)$, and $d(\mathcal{R}_{\boldsymbol{q}}, \mathcal{O}_j)$] are computed using a simplified model of the robot and the obstacles based on planes, spheres and capsules).

Note that as opposed to the potential-field function presented in [13], which was valid only for the motion planning of a free-flying robot with only translation DOFs, in this paper the potential field has been extended to scenarios with a dual-arm robotic system (with more and different DOF types), and it could be extended easily to problems with several dual-arm mobile manipulators (i.e., parallel articulated systems with many DOFs of any type).

B. HD-RRT* Planner

The proposed planning algorithm, called human demonstrated RRT* (HD-RRT*), is based on the RRT* planner [11] that has as parameters the sampling bias α toward the goal configuration and the advance step ϵ used in the extend function to grow the tree.

In order to cope with the limitations of the standard RRT* for high-dimensional configuration spaces, a modified version was proposed with the following changes [45].

1) *A Sampling Bias:* Once a solution has been found, the sampling is biased, with a given probability β, toward configurations around it. This guides the paths toward local optimal solutions.
2) *A Node-Rejection Criteria:* Those samples that may not be useful in finding a better solution than the current one are discarded. This keeps the tree as reduced as possible, thus reducing the computational cost.

The HD-RRT* planner proposed here introduces the next additional changes with respect to the modified RRT*.

1) *The Optimization Function:* The minimization of this function, computed using (1)–(6), guides the solution toward short paths that follow as much as possible the demonstrated movements and that move away from obstacles and from self-collisions.
2) *The Extension Procedure:* In the standard RRT* growth of the tree, the selected node is steered toward the sampled configuration. Here, this is modified to steer the

---

Algorithm 1: CSTEER

> **Input** : Configurations q_{near}, q_{rand}
> **Output:** Configuration q_{new}

1: **if** RAND01() $\geq \gamma$ **then**
2: | **return** $q_{\text{near}} + \min(\epsilon, \|q_{\text{rand}} - q_{\text{near}}\|)$ UNIT$(q_{\text{rand}} - q_{\text{near}})$
3: $\omega \leftarrow (\omega_P + \omega_I + \omega_D)$ RAND01()
4: **if** $\omega < \omega_P$ **then**
5: | **return** $q_{\text{near}} + \min(\epsilon, \|q_{\text{goal}} - q_{\text{near}}\|)$ UNIT$(q_{\text{goal}} - q_{\text{near}})$
6: **else if** $\omega \in [\omega_P, \omega_P + \omega_I]$ **then**
7: | **return** $q_{\text{near}} - \epsilon$ UNIT$(\triangledown V(q_{\text{near}}))$
8: **else**
9: | **return** $q_{\text{near}} + \epsilon$ RANDORTHNORM$(\triangledown V(q_{\text{near}}))$
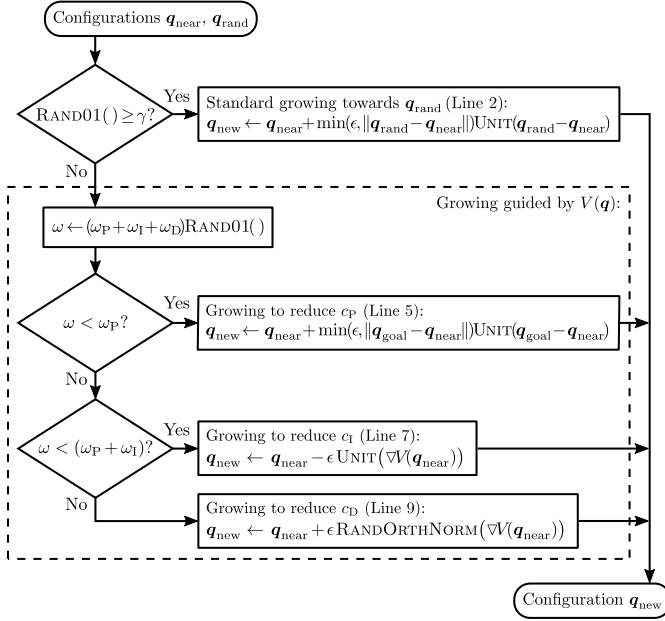

Fig. 3.   Pseudocode and flowchart of the CSTEER algorithm.

node with a probability γ toward low-cost directions (with a stochastic gradient-descent method) using the function CSTEER detailed below.

The proposed HD-RRT* planning algorithm uses the procedure CSTEER to extend the tree from a given configuration q_{near}. The pseudocode and the flowchart of CSTEER are shown in Fig. 3, where the following functions are used.

1) RAND01() returns a value uniformly chosen at random from the interval [0, 1].
2) UNIT(v) returns $(v/\|v\|)$ if $\|v\| \neq 0$, and v otherwise.
3) RANDORTHNORM(v) returns a random, unitary vector orthogonal to v if $\|v\| \neq 0$, and v otherwise.
4) $V(q)$ is the potential-field value computed using (2).
5) $\triangledown V(q_{near})$ denotes the gradient of $V(q)$ evaluated at q_{near}.

The extension is performed toward q_{rand} with an incremental step ϵ (line 2), as it is done in the standard RRT algorithm. However, with a probability $\gamma < 1$, a stochastic gradient-descent method minimizing the motion cost is applied instead. Note that the gradient-descent method can be trapped in local minima of the motion cost. Nevertheless, since the gradient descent is not applied always in all the iterations, the RRT* exploration properties are preserved and the possible

local minimum traps are avoided (assuming $\gamma < 1$). The extension direction is chosen randomly (line 3) between the directions that minimize each component of the motion cost, i.e., c_P, c_I, and c_D [see (1)]. Each of these cost components is chosen to be minimized with a probability proportional to its weight value ω_P, ω_I, and ω_D, respectively (e.g., the greater ω_P regarding ω_I and ω_D, the greater the probability that the tree grows in the direction that minimizes c_P). Then:

1) since c_P measures the path length, the direction pointing from q_{near} toward q_{goal} minimizes c_P (line 5);
2) since c_I measures the average value of the potential field along the path, and the gradient $\triangledown V(q)$ of the potential field points in the direction of the local greatest growth of $V(q)$, then the direction that minimizes c_I points in the opposite direction of $\triangledown V(q)$, i.e., the direction in which $V(q)$ locally decreases (line 7);
3) since c_D measures the variations of $V(q)$ along the motion, then any direction orthogonal to $\triangledown V(q)$ minimizes c_D because $V(q)$ does not locally grow in any direction perpendicular to $\triangledown V(q)$ (line 9).

After several tests with different tasks, the parameters of the HD-RRT* algorithm have been empirically set to $\alpha = 0.05$, $\beta = 0.1$, and $\gamma = 0.1$, being ϵ dependant on the task. Regarding the motion-cost function, the motion connecting straightly q_{start} and q_{goal} has been used to set each weight of the motion-cost function: $\omega_\Gamma = c_\Gamma(q_{start}, q_{goal})^{-1}$ for $\Gamma \in \{P, I, D\}$ [see (1)]. Besides, the parameters of the potential fields have been empirically set to: $\lambda_{\text{goal}} = 0.1$, $\sigma_{\text{goal}} = 0.1$; $\lambda_i = 0.1$, $\sigma_i = 7 \,\forall i$; $\lambda_{\text{arms}} = 0.3$, $\sigma_{\text{arms}} = 10$; and $\lambda_j = 0.3$, $\sigma_j = 10 \,\forall j$ [see (3)–(6)]. The sensibility of the system performance with respect to the planner parameters is not high, thus determining them is not a critical issue. Thereby, the same values of the parameters are used in the conceptual and the real examples presented in the next section, with the exception of the parameter ϵ that is the unique task-dependant parameter.

C. Validation and Performance Analysis

The approach has been implemented within the Kautham project [46], a motion planning and simulation framework for teaching and research. The experiments described below were obtained running the planner in a 2.13-GHz Intel 2, 4-GB RAM PC.

First, for illustrative purposes, a simple example has been set up. It consists of a 2-D scenario where a two-link planar manipulator must go from the start configuration q_{start} to the goal configuration q_{goal} avoiding collisions with circular obstacles (see Fig. 4). Three demonstration paths and q_{goal} were used to generate the attractive potential field, while the circular obstacles generate repulsive potential fields. The combination of these attractive and repulsive potential fields forms the potential-field function $V(q)$. Fig. 4(left) shows the three demonstration paths in the problem space and Fig. 4(right) shows the obtained solution. Fig. 5 shows resulting potential-field function $V(q)$ in the configuration space, including the three demonstration paths in Fig. 5(left) and the resulting tree of samples and the obtained solution in Fig. 5(right).
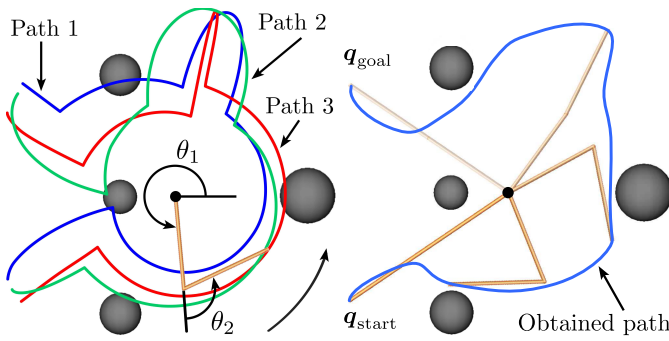
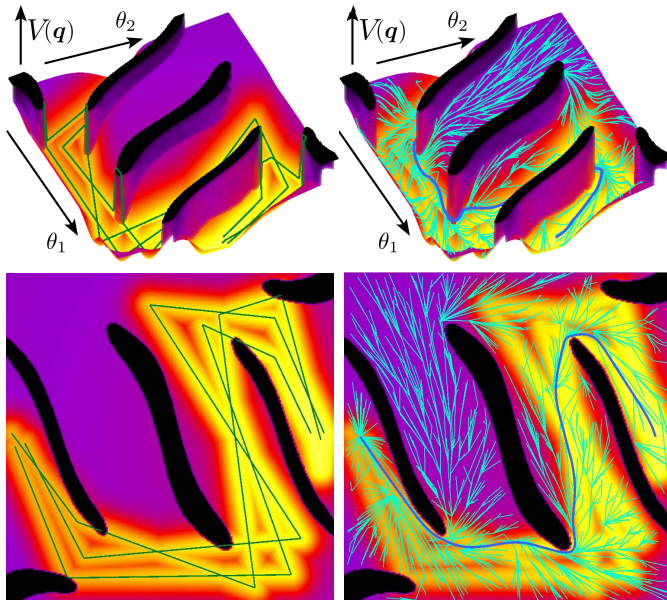Fig. 4. Two-link planar manipulator problem: demonstrated paths (left) and obtained solution path (right).

Fig. 5. Tridimensional and top views of the potential field $V(\boldsymbol{q})$ over the configuration space $\mathcal{C}$ for the example in Fig. 4 [brighter colors represent lower values of $V(\boldsymbol{q})$], with the demonstrated paths (left), and the obtained solution path and sample tree (right).

Note that $V(\boldsymbol{q})$ is shaped like a plateau in the regions of $\mathcal{C}$ where the manipulator is in collision with the obstacles (depicted in black in Fig. 5), while, on the other hand, the demonstration paths originate valleys (bright colored in Fig. 5). Therefore, the use of $V(\boldsymbol{q})$ in the c_I and c_D cost components in (1) enforce the solution path to follow the demonstrations as close as possible, while c_P tries to shorten the path.

The planning procedure assures that a solution path avoiding obstacles and self-collisions is found (if one exists) due to the asymptotic completeness of any RRT-based planning algorithm, even if the demonstration paths are not collision-free (as it actually happens in this example, see Figs. 4 and 5). It must be also remarked that the fact that the demonstration paths provides relevant information on a given task is more significant than the number of demonstration paths used, and that the method works well even with a single demonstration (in this case the valleys are sharper, and they become wider when there are several different demonstration paths, with the valley width growing when the dispersion of the demonstration

Time first solution	Path length	Total cost $c_{\mathcal{P}}$	Unit cost $\hat{c}_{\mathcal{P}}$
0.26 s	10.825 rad	1.195	0.111

Planning space / Dimension	$\mathcal{C}$ / 12	B_k / 2
Used time [s]	100	10
Time first solution [s]	1.35	0.33
Solution length [rad]	5.513	5.141
Total cost $c_{\mathcal{P}}$	1.095	1.186
Unit cost $\hat{c}_{\mathcal{P}}$	0.199	0.231
Tree growing success [%]	73.49	94.56

paths grows). On the other hand, the computation time of the motion-cost function grows when the number of demonstration paths increases [as it is expected according to (4)], but it does not produce any other negative consequence.

Numerical results of the two-link planar manipulation problem using three demonstration paths are summarized in Table I where the average values after 100 executions are shown (remind that the sampling-based planners rely on a random process and therefore generate a different solution each execution). A maximum time of 10 s was allowed for each execution, this was enough to get a 100% of success rate, i.e., the system finds always a collision-free path avoiding self-collisions and collisions with the obstacles. The collected data include the following.

1) The final solution length L (measured in $\mathcal{C}$ as the summation of joint movements in radians).
2) The final path cost $c_{\mathcal{P}}$ (defined as the sum of the motion costs of all the segments that form the path).
3) The unit path cost $\hat{c}_{\mathcal{P}}$ (computed as $c_{\mathcal{P}}$ divided by L).

After this simple example, the planning of the motions for an *assembly task* is used as a real example of the proposed planning procedure (see Fig. 1). This task consists in holding a cylindrical box with one hand and a soda can with the other, and then move both objects to a preassembly pose that allows the insertion of the can into the box. Note that the start and the goal dual-arm configurations are given and that the proposed algorithm plans the path of the whole dual-arm robotic system. For this example, the movements of a human operator were captured while solving the task (see Fig. 1), and then these movements were mapped to the dual-arm system (see Section III-A). These human movements were used as demonstration paths to generate the attractive potential fields as well as to obtain the zero-order basis ^0S of the demonstrated task. The axes of ^0S are sorted in decreasing order of the associated sample dispersions, then the subspace B_k spanned by the first k axes has a dimension lower than the complete $\mathcal{C}$ space and, at the same time, contains a high percentage of the sample variance. In this paper, k has been chosen so that the accumulated sample variance of the first k axes surpasses the 95% of the total sample variance, i.e., k depends on the human demonstrations of the task and it may vary from task to task. Following this criterion, for this example, only two
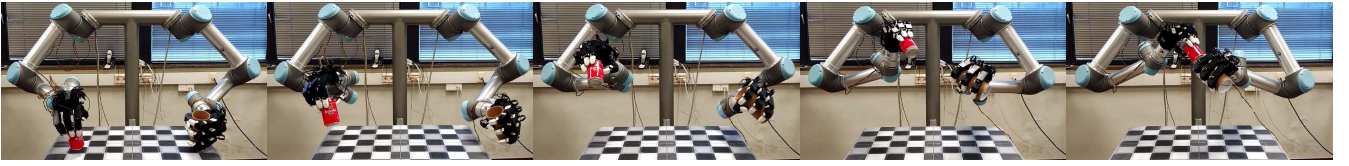
Fig. 6. Snapshots of a solution path for the assembly example planned in the reduced subspace B_k.

axes were needed [Fig. 1(bottom-right) shows the distribution of the accumulated sample variance of the captured motion as a function of the number of synergies]. The potential field was generated using five demonstration paths, and the planning of the robot motions has been done using the whole configuration space $\mathcal{C}$ and also using the reduced planning subspace B_k, with maximum allowed planning times of 100 and 10 s, respectively, assuring a 100% of success rate.

Fig. 6 shows snapshots of an instance of the solution path for the assembly task obtained using the reduced subspace B_k. Videos of each step of the experiment for the assembly task are available in [47]. Table II shows the average results obtained after 100 executions for each case using five demonstration paths. The table includes, as *tree growing success*, the percentage of times that the CSTEER function returned a collision-free motion (i.e., the percentage of iterations in which no collisions occur and the tree actually grows).

As expected, the best paths (the ones with the lowest cost) are obtained when the whole $\mathcal{C}$ space was used. Nevertheless, planning in B_k allows a much shorter planning time (due to the reduced dimension of the subspace) without incrementing excessively the cost of the path. In addition, the use of B_k increases the probability of obtaining collision-free configurations (see the *tree growing success* in Table II) because fewer self-collisions occur, and therefore the efficiency of the planning procedure increases.

V. HUMAN-LIKENESS EVALUATION

A. Definition of Human-Likeness Index

The proposed planning algorithm tries to mimic the human demonstrations (which does not mean "following a specific human path") as long as it does not imply that the arms are dangerously close to each other or to the obstacles. In addition, the goal configuration acts as an attractive point for the planned path. Therefore, the planned path does not follow strictly the human demonstrated motion and then the human-likeness of the planned path may be somehow spoiled. In order to evaluate the human-likeness of different paths (obtained with the proposed planning procedure or with any other), this paper introduces a human-likeness index $\mathcal{Q}_\mathcal{P}$. This index computes the misalignment of a path with respect to the first-order bases ^1S obtained from human movements. Since as detailed in Section III-B, the configuration space is split into cells, each one having an associated ^1S basis, the value $\mathcal{Q}_\mathcal{P}$ of a path $\mathcal{P}$ is computed as

$$\mathcal{Q}_\mathcal{P} = 1 - \frac{1}{L}\int_\mathcal{P} \text{MISALIGNMENT}(\boldsymbol{q}, \boldsymbol{v})\, \mathrm{d}\boldsymbol{q} \qquad (7)$$

where L is the path length, $\boldsymbol{v} = \dot{\boldsymbol{q}}$, and $\text{MISALIGNMENT}(\boldsymbol{q}, \boldsymbol{v})$ is the function that returns the misalignment η of the direction $\boldsymbol{v}$

with respect to the basis $^1S(\boldsymbol{\mu}, \Sigma)$ of the cell where $\boldsymbol{q}$ lies. This misalignment η is measured as

$$\eta = \frac{1}{\pi}\text{acos}\big((1 - \rho)\Phi_{\boldsymbol{\mu}} + \rho\Phi_\Sigma\big) \qquad (8)$$

where

- $\rho \in [0, 1]$ is a weighting variable that represents the proximity of the basis $^1S(\boldsymbol{\mu}, \Sigma)$ to the origin of the velocity space, i.e., ρ increases as the origin of ^1S gets closer to the origin of the velocity space. ρ is computed as two times the probability P that a random vector $\boldsymbol{x}$ obtained from the normal multivariate distribution $\mathcal{N}(\boldsymbol{\mu}, \Sigma)$ (i.e., with barycenter $\boldsymbol{\mu}$ and covariance matrix Σ) satisfies $\boldsymbol{\mu} \cdot \boldsymbol{x} < 0$. The probability P is given by

$$P(\boldsymbol{\mu} \cdot \boldsymbol{x} < 0 | \boldsymbol{x} \sim \mathcal{N}(\boldsymbol{\mu}, \Sigma)) = \frac{1}{2} - \frac{1}{2}\text{erf}\left(\frac{\boldsymbol{\mu} \cdot \boldsymbol{\mu}}{\sqrt{2\boldsymbol{\mu}^\mathsf{T}\Sigma\boldsymbol{\mu}}}\right) \qquad (9)$$

where $\text{erf}(x)$ is the error function. Then

$$\rho = 1 - \text{erf}\left(\frac{\boldsymbol{\mu} \cdot \boldsymbol{\mu}}{\sqrt{2\boldsymbol{\mu}^\mathsf{T}\Sigma\boldsymbol{\mu}}}\right). \qquad (10)$$

Therefore, when the first-order basis ^1S is exactly centered at the origin (i.e., $\|\boldsymbol{\mu}\| = 0$), half of the distribution $\mathcal{N}$ satisfies the inequality and, hence, $\rho = 1$. As the first-order basis ^1S gets away from the origin (i.e., $\|\boldsymbol{\mu}\| \to \infty$), only a reduced region of $\mathcal{N}$ satisfies the inequality and, therefore, $\rho \to 0$.

- $\Phi_{\boldsymbol{\mu}} \in [-1, 1]$ is a measure that represents the alignment between $\boldsymbol{v}$ and $\boldsymbol{\mu}$ [see Fig. 7(left)].
  $\Phi_{\boldsymbol{\mu}}$ is computed as

$$\Phi_{\boldsymbol{\mu}} = \text{sgn}(\boldsymbol{v} \cdot \boldsymbol{\mu})e^{-\frac{1}{2}(\boldsymbol{w} - \boldsymbol{\mu})^\mathsf{T}\Sigma^{-1}(\boldsymbol{w} - \boldsymbol{\mu})} \qquad (11)$$

where $\text{sgn}(x)$ is the sign function. $\Phi_{\boldsymbol{\mu}}$ is positive if $(\boldsymbol{v} \cdot \boldsymbol{\mu}) > 0$, and negative otherwise. Besides, $|\Phi_{\boldsymbol{\mu}}|$ is proportional to the value of the probability density function of $\mathcal{N}(\boldsymbol{\mu}, \Sigma)$ evaluated at $\boldsymbol{w}$, which is a scaled version of $\boldsymbol{v}$ so that the projection of $\boldsymbol{w}$ into $\boldsymbol{\mu}$ is $\boldsymbol{\mu}$ itself [see Fig. 7(left)], i.e., $\boldsymbol{w} = (\boldsymbol{\mu} \cdot \boldsymbol{\mu}/\boldsymbol{v} \cdot \boldsymbol{\mu})\boldsymbol{v}$. Therefore, $|\Phi_{\boldsymbol{\mu}}| = 1$ when $\boldsymbol{v}$ and $\boldsymbol{\mu}$ are parallel and $|\Phi_{\boldsymbol{\mu}}| = 0$ when $\boldsymbol{v}$ and $\boldsymbol{\mu}$ are orthogonal.

- $\Phi_\Sigma \in [-1, 1]$ is a measure that represents the alignment of $\boldsymbol{v}$ and the direction $\boldsymbol{u}_1$ of largest variance of Σ [see Fig. 7(right)].
  Φ_Σ is computed as

$$\Phi_\Sigma = 2\frac{\hat{\boldsymbol{v}}^\mathsf{T}\Sigma\hat{\boldsymbol{v}}}{\boldsymbol{u}_1^\mathsf{T}\Sigma\boldsymbol{u}_1} - 1 \quad \text{with} \quad \hat{\boldsymbol{v}} = \frac{\boldsymbol{v}}{\|\boldsymbol{v}\|} \qquad (12)$$

where $\hat{\boldsymbol{v}}^\mathsf{T}\Sigma\hat{\boldsymbol{v}}$ is the variance of Σ in the direction of $\boldsymbol{v}$, and $\boldsymbol{u}_1^\mathsf{T}\Sigma\boldsymbol{u}_1$ is the variance of Σ in the direction of $\boldsymbol{u}_1$.
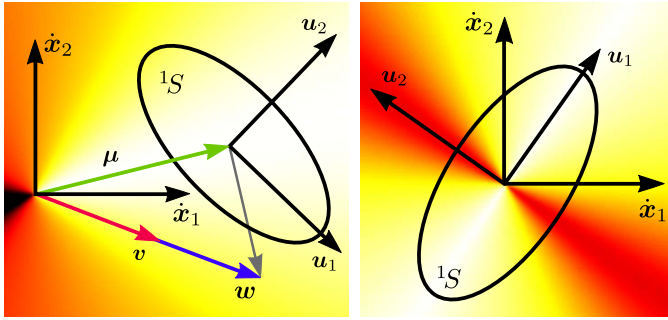
Fig. 7. Misalignment of each direction $v = [\dot{x}_1, \dot{x}_2]$, when the first-order basis $^1S(\mu, \Sigma)$ is far from the origin, i.e., $\Phi \approx \Phi_\mu$ (left), and when ^1S is exactly centered at the origin, i.e., $\Phi = \Phi_\Sigma$ (right). Brighter colors denote better alignments. Σ is represented by an ellipse oriented according to the eigenvectors u_i of Σ and with semiaxes proportional to the square roots of the eigenvalues of Σ. A sample of the velocities v and w is also shown.

The quotient of these two variances takes the maximum value 1 when v and u_1 are parallel, and the minimum value 0 when v is parallel to u_m, the direction of smallest variance of Σ. To obtain Φ_Σ, this quotient is then expanded from the interval $[0, 1]$ to the interval $[-1, 1]$ with a linear transformation.

Note that the misalignment value $\eta \in [0, 1]$ and it is small when the advance direction v is similar to the synergy directions. When the difference between v and the synergy directions increases, the misalignment increases.

The pseudocode and the flowchart of the MISALIGNMENT function are shown in Fig. 8. First, the first-order synergy basis $^1S(\mu, \Sigma)$ of the cell where q lies is obtained with the function FOSBASIS(q) (line 1) which returns $\emptyset$ if no first-order basis is available, i.e., q is outside $B(^0S_G)$ and therefore it does not belong to any cell (see Section III-B). If $^1S = \emptyset$ the misalignment η is set to the maximum value 1 (line 2); otherwise, ρ is computed following (10) (line 4), Φ_μ is computed according to (11) (line 5), and Φ_Σ is computed according to (12) (line 6). Finally, η is computed according to (8) (line 7).

Now, since the path $\mathcal{P}$ is composed of a sequence of n consecutive configurations q_i connected by rectilinear motions, $\mathcal{Q}_\mathcal{P}$ from (7) can be approximated as

$$\mathcal{Q}_\mathcal{P} \approx 1 - \sum_{i=1}^{n-1} \text{MISALIGNMENT}(q_i, q_{i+1} - q_i) \frac{\|q_{i+1} - q_i\|}{L}. \tag{13}$$

Therefore a path with a high $\mathcal{Q}_\mathcal{P}$ value, is highly aligned in $\mathcal{C}$ with the human movements. Then, if the robot kinematic structure is anthropomorphic (and the similar to the human operator, the better), the position and velocity of the robot wrists and the human wrists are similar.

The human-likeness index $\mathcal{Q}_\mathcal{P}$ depends on the ^1S bases used. $\mathcal{Q}_\mathcal{P}$ can be tailored to any given particular task by using the corresponding ^1S bases, and used for the evaluation of the human-likeness of the execution of that particular task. Note that the ^1S bases depend on the mapping of the human movements to the robot configuration space, thus a mapping preserving the human-likeness should be used to make ^1S really represent the human-like movements.

Algorithm 2: MISALIGNMENT function

> **Input** : Configuration q and advance direction v
> **Output:** Misalignment value η of moving from q in the direction v

1: $^1S(\mu, \Sigma) \leftarrow$ FOSBASIS(q)
2: **if** $^1S = \emptyset$ **then** $\eta \leftarrow 1$
3: **else**
4:    Compute ρ according to Eq. (10)
5:    Compute Φ_μ according to Eq. (11)
6:    Compute Φ_Σ according to Eq. (12)
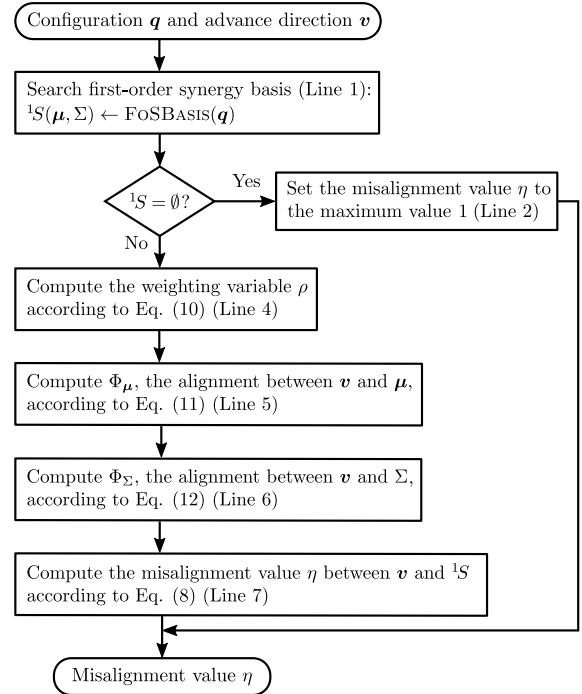7:   Compute η according to Eq. (8)
8: **return** η

Fig. 8. Pseudocode and flowchart of the MISALIGNMENT function.

In this paper, we propose the use of ^1S obtained from natural *free-movements* of the operator while he/she freely moves both arms and hands in an unconstrained way (i.e., without performing any specific task) trying to cover the whole workspace in front of the body. There is no guarantee that the operator actually covers the whole workspace, but it is expected that he/she performs his/her most natural and evident movements.

B. Evaluation

Zero- and first-order synergy bases were computed using the *free-movements* described above. The configuration space $\mathcal{C}$ was split into 64 cells based on the synergy differences, i.e., a first-order basis ^1S was assigned to each cell of $\mathcal{C}$. These bases were used for the computation of $\mathcal{Q}_\mathcal{P}$, which was applied to the evaluation of the human-likeness of the solutions found for the assembly example defined in Section III-A using the following cases.

  a) The HD-RRT* planner with several demonstrations, planning in the whole configuration space $\mathcal{C}$.
  b) The HD-RRT* planner with several demonstrations, planning in the lower-dimensional subspace B_k.

TABLE III
AVERAGE HUMAN-LIKENESS VALUE OF THE ASSEMBLY EXAMPLE
USING THE PRESENTED APPROACH WITH SEVERAL
DEMONSTRATIONS [CASES a) AND b)], A SIMILAR
APPROACH [CASE c)], THE RRT [CASES d) AND e)],
AND AN ARTIFICIAL PATH [CASE f)]

Case	Planning dim.	Used time [s]	Path length [rad]	Quality $\mathcal{Q}_\mathcal{P}$
a)	12	100	5.513	0.594
b)	2	10	5.141	0.573
c)	4	0.35	4.990	0.465
d)	12	32.39	6.647	0.433
e)	2	18.38	5.965	0.428
f)	-	-	17.452	0.045

c) The planner introduced in [34], that simply computes zero-order synergies for different tasks and uses them to reduce the dimension of the search space, thus reducing the computational cost.

d) The standard RRT planner [6], planning in the whole configuration space $\mathcal{C}$.

e) The standard RRT planner, planning in the lower-dimensional subspace B_k.

f) Two rectilinear segments in $\mathcal{C}$ connecting the start and the goal configurations through an empirically selected configuration $\boldsymbol{q}_m \notin B(^0S_G)$, i.e., $\boldsymbol{q}_m$ is not in the subspace of the sampled configurations of the *free-movements*. Note that in this case no motion planning is performed but even so the path is checked to be free of collisions, either involving the obstacles or both robotic arms.

Table III shows the average results obtained, for each case, after 100 executions. It can be noted that the proposed planner obtains paths with a significant better $\mathcal{Q}_\mathcal{P}$ quality (even though the presented approach needs a longer planning time), i.e., the proposed procedure finds solution paths that are better aligned with the natural movements of the human operator and that therefore are more human-like. Note that the approach presented in this paper obtains a better $\mathcal{Q}_\mathcal{P}$ even though the human movements used in the motion planning are different to the ones used to compute $\mathcal{Q}_\mathcal{P}$. The path with the greatest quality is obtained when the motions are planned in the whole $\mathcal{C}$ space. However, the use of the subspace B_k is the best option since it reduces significantly the computational cost without penalizing considerably $\mathcal{Q}_\mathcal{P}$. Case (c) is very fast since it is not based in any optimization method and hence ends as soon as a solution is found, and has a relative good $\mathcal{Q}_\mathcal{P}$. The poorest quality is obtained with the manually set path, denoting that this path is not much human-like. The planner used in cases (d) and (e) does not consider human-likeness nor path length as a quality index. Hence, bad results are obtained for both measures.

Videos of paths obtained for the assembly task with the considered approaches are available in [47].

VI. CONCLUSION

This paper has introduced a motion planning procedure, designed for anthropomorphic dual-arm robotic systems, that allows to solve manipulation tasks in a human-like fashion. To this end, the movements of a human operator have been used to generate attractive potential fields over the configuration space. The motion planning has been solved with an RRT*-based algorithm, with a stochastic gradient descent method to minimize a motion cost. The algorithm navigates through the potential fields and biases the tree growth toward the human-like movements. In addition, the synergies (couplings between DOFs) of the demonstration movements have been computed to find a lower-dimensional subspace where the motion planning can be solved more efficiently, basically due to the fact that the sampling procedure produces in fewer self-collision configurations. The proposed approach has been illustrated with a conceptual example and a real example executed with a physical dual-arm robotic system. A human-likeness index, based on first-order synergies (correlations between joint velocities) obtained from human movements, has been also proposed and used for comparisons. The obtained results show that the proposed procedure obtains paths that are more human-like.

As a conclusion, this paper has presented a simple yet efficient way to compute paths for dual-arm robotic systems with human-like appearance, and it opens interesting potential research lines, such as the use of demonstration paths in the joint-velocity space and their first-order synergies during the motion planning. Another interesting research direction concerns the optimization of the presented human-likeness index while solving the motion planning in order to better mimic human task executions.

REFERENCES

[1] B. Tovar, R. Murrieta-Cid, and S. M. LaValle, "Distance-optimal navigation in an unknown environment without sensing distances," *IEEE Trans. Robot.*, vol. 23, no. 3, pp. 506–518, Jun. 2007.

[2] H. Wang, Y. Chen, and P. Soueres, "A geometric algorithm to compute time-optimal trajectories for a bidirectional steered robot," *IEEE Trans. Robot.*, vol. 25, no. 2, pp. 399–413, Apr. 2009.

[3] T. Fukuda *et al.*, "How far away is 'artificial man,'" *IEEE Robot. Autom. Mag.*, vol. 8, no. 1, pp. 66–73, Mar. 2001.

[4] M. Elbanhawi and M. Simic, "Sampling-based robot motion planning: A review," *IEEE Access*, vol. 2, pp. 56–77, 2014.

[5] L. E. Kavraki, P. Svestka, J.-C. Latombe, and M. H. Overmars, "Probabilistic roadmaps for path planning in high-dimensional configuration spaces," *IEEE Trans. Robot. Autom.*, vol. 12, no. 4, pp. 566–580, Aug. 1996.

[6] J. J. Kuffner and S. M. LaValle, "RRT-connect: An efficient approach to single-query path planning," in *Proc. IEEE Int. Conf. Robot. Autom.*, San Francisco, CA, USA, Apr. 2000, pp. 995–1001.

[7] M. Stilman, "Global manipulation planning in robot joint space with task constraints," *IEEE Trans. Robot.*, vol. 26, no. 3, pp. 576–584, Jun. 2010.

[8] L. Jaillet, J. Cortés, and T. Siméon, "Sampling-based path planning on configuration-space costmaps," *IEEE Trans. Robot.*, vol. 26, no. 4, pp. 635–646, Aug. 2010.

[9] J. Lee, O. Kwon, L. Zhang, and S.-E. Yoon, "A selective retraction-based RRT planner for various environments," *IEEE Trans. Robot.*, vol. 30, no. 4, pp. 1002–1011, Aug. 2014.

[10] J. Rosell, R. Suárez, and A. Pérez, "Path planning for grasping operations using an adaptive PCA-based sampling method," *Auton. Robots*, vol. 35, no. 1, pp. 27–36, Jul. 2013.

[11] S. Karaman and E. Frazzoli, "Sampling-based algorithms for optimal motion planning," *Int. J. Robot. Res.*, vol. 30, no. 7, pp. 846–894, Jun. 2011.

[12] A. H. Qureshi *et al.*, "Potential guided directional-RRT* for accelerated motion planning in cluttered environments," in *Proc. IEEE Int. Conf. Mechatronics Autom.*, Takamatsu, Japan, Aug. 2013, pp. 519–524.

[13] N. García, R. Suárez, and J. Rosell, "HG-RRT*: Human-guided optimal random trees for motion planning," in *Proc. IEEE Int. Conf. Emerg. Technol. Factory Autom.*, Luxembourg, Luxembourg, Sep. 2015, pp. 1–7.

[14] S. M. Khansari-Zadeh and O. Khatib, "Learning potential functions from human demonstrations with encapsulated dynamic and compliant behaviors," *Auton. Robots*, vol. 41, no. 1, pp. 45–69, Jan. 2017.

[15] S. Cho and S. Jo, "Incremental online learning of robot behaviors from selected multiple kinesthetic teaching trials," *IEEE Trans. Syst., Man, Cybern., Syst.*, vol. 43, no. 3, pp. 730–740, May 2013.

[16] N. Fligge, J. McIntyre, and P. van der Smagt, "Minimum jerk for human catching movements in 3D," in *Proc. IEEE RAS/EMBS Int. Conf. Biomed. Robot. Biomechatron.*, Rome, Italy, 2012, pp. 581–586.

[17] A. Piazzi and A. Visioli, "Global minimum-jerk trajectory planning of robot manipulators," *IEEE Trans. Ind. Electron.*, vol. 47, no. 1, pp. 140–149, Feb. 2000.

[18] M. D. Breteler, S. C. Gielen, and R. G. Meulenbroek, "End-point constraints in aiming movements: Effects of approach angle and speed," *Biol. Cybern.*, vol. 85, no. 1, pp. 65–75, Jul. 2001.

[19] S. Albrecht *et al.*, "Imitating human reaching motions using physically inspired optimization principles," in *Proc. IEEE RAS Int. Conf. Humanoid Robots*, Bled, Slovenia, Oct. 2011, pp. 602–607.

[20] W. Park, D. B. Chaffin, and B. J. Martin, "Toward memory-based human motion simulation: Development and validation of a motion modification algorithm," *IEEE Trans. Syst., Man, Cybern. A, Syst., Humans*, vol. 34, no. 3, pp. 376–386, May 2004.

[21] C. Rigotti, P. Cerveri, G. Andreoni, A. Pedotti, and G. Ferrigno, "Modeling and driving a reduced human mannequin through motion captured data: A neural network approach," *IEEE Trans. Syst., Man, Cybern. A, Syst., Humans*, vol. 31, no. 3, pp. 187–193, May 2001.

[22] T. Tsuji, Y. Tanaka, and M. Kaneko, "Bio-mimetic trajectory generation based on human arm movements with a nonholonomic constraint," *IEEE Trans. Syst., Man, Cybern. A, Syst., Humans*, vol. 32, no. 6, pp. 773–779, Nov. 2002.

[23] Z. Zhang, Z. Li, Y. Zhang, Y. Luo, and Y. Li, "Neural-dynamic-method-based dual-arm CMG scheme with time-varying constraints applied to humanoid robots," *IEEE Trans. Neural Netw. Learn. Syst.*, vol. 26, no. 12, pp. 3251–3262, Dec. 2015.

[24] Z. Li, K. Yang, S. Bogdan, and B. Xu, "On motion optimization of robotic manipulators with strong nonlinear dynamic coupling using support area level set algorithm," *Int. J. Control Autom. Syst.*, vol. 11, no. 6, pp. 1266–1275, Dec. 2013.

[25] X. Ding and C. Fang, "A novel method of motion planning for an anthropomorphic arm based on movement primitives," *IEEE/ASME Trans. Mechatronics*, vol. 18, no. 2, pp. 624–636, Apr. 2013.

[26] J. Romero, T. Feix, C. H. Ek, H. Kjellström, and D. Kragic, "Extracting postural synergies for robotic grasping," *IEEE Trans. Robot.*, vol. 29, no. 6, pp. 1342–1352, Dec. 2013.

[27] M. T. Ciocarlie and P. K. Allen, "Hand posture subspaces for dexterous robotic grasping," *Int. J. Robot. Res.*, vol. 28, no. 7, pp. 851–867, Jul. 2009.

[28] N. Hogan and D. Sternad, "Dynamic primitives of motor behavior," *Biol. Cybern.*, vol. 106, nos. 11–12, pp. 727–739, Dec. 2012.

[29] J. Rosell and R. Suárez, "Using hand synergies as an optimality criterion for planning human-like motions for mechanical hands," in *Proc. IEEE RAS Int. Conf. Humanoid Robots*, Madrid, Spain, Nov. 2014, pp. 232–237.

[30] F. Ficuciello, G. Palli, C. Melchiorri, and B. Siciliano, "Postural synergies of the UB hand IV for human-like grasping," *Robot. Auton. Syst.*, vol. 62, no. 4, pp. 515–527, Apr. 2014.

[31] M. Gabiccini, A. Bicchi, D. Prattichizzo, and M. Malvezzi, "On the role of hand synergies in the optimal choice of grasping forces," *Auton. Robots*, vol. 31, nos. 2–3, pp. 235–252, Oct. 2011.

[32] G. Palli *et al.*, "The DEXMART hand: Mechatronic design and experimental evaluation of synergy-based control for human-like grasping," *Int. J. Robot. Res.*, vol. 33, no. 5, pp. 799–824, Apr. 2014.

[33] D. Prattichizzo, M. Malvezzi, M. Gabiccini, and A. Bicchi, "On motion and force controllability of precision grasps with hands actuated by soft synergies," *IEEE Trans. Robot.*, vol. 29, no. 6, pp. 1440–1456, Dec. 2013.

[34] R. Suárez, J. Rosell, and N. García, "Using synergies in dual-arm manipulation tasks," in *Proc. IEEE Int. Conf. Robot. Autom.*, Seattle, WA, USA, May 2015, pp. 5655–5661.

[35] N. García, R. Suárez, and J. Rosell, "Task-dependent synergies for motion planning of an anthropomorphic dual-arm system," *IEEE Trans. Robot.*, vol. 33, no. 3, pp. 756–764, Jun. 2017.

[36] J. Cui, Y. Liu, Y. Xu, H. Zhao, and H. Zha, "Tracking generic human motion via fusion of low-and high-dimensional approaches," *IEEE Trans. Syst., Man, Cybern., Syst.*, vol. 43, no. 4, pp. 996–1002, Jul. 2013.

[37] L. Colasanto, R. Suárez, and J. Rosell, "Hybrid mapping for the assistance of teleoperated grasping tasks," *IEEE Trans. Syst., Man, Cybern., Syst.*, vol. 43, no. 2, pp. 390–401, Mar. 2013.

[38] T. Kondo, O. Amagi, and T. Nozawa, "Proposal of anticipatory pattern recognition for EMG prosthetic hand control," in *Proc. IEEE Int. Conf. Syst. Man Cybern.*, Oct. 2008, pp. 897–902.

[39] N. García, J. Rosell, and R. Suárez, "Motion planning using first-order synergies," in *Proc. IEEE/RSJ Int. Conf. Intell. Robots Syst.*, Singapore, Sep. 2015, pp. 2058–2063.

[40] N. García, R. Suárez, and J. Rosell, "First-order synergies for motion planning of anthropomorphic dual-arm robots," in *Proc. IFAC World Congr.*, Jul. 2017, pp. 2283–2290.

[41] M. V. Liarokapis, P. K. Artemiadis, and K. J. Kyriakopoulos, "Functional anthropomorphism for human to robot motion mapping," in *Proc. IEEE Int. Symp. Robot Human Interact. Commun.*, Paris, France, Sep. 2012, pp. 31–36.

[42] W. Chen, C. Xiong, and S. Yue, "Mechanical implementation of kinematic synergy for continual grasping generation of anthropomorphic hand," *IEEE/ASME Trans. Mechatronics*, vol. 20, no. 3, pp. 1249–1263, Jun. 2015.

[43] T. Wimböck, B. Jan, and G. Hirzinger, "Synergy level impedance control for multifingered hand," in *Proc. IEEE/RSJ Int. Conf. Intell. Robots Syst.*, San Francisco, CA, USA, Sep. 2011, pp. 973–979.

[44] J. Steffen, R. Haschke, and H. Ritter, "Towards dextrous manipulation using manipulation manifolds," in *Proc. IEEE/RSJ Int. Conf. Intell. Robots Syst.*, Nice, France, Sep. 2008, pp. 2738–2743.

[45] B. Akgun and M. Stilman, "Sampling heuristics for optimal motion planning in high dimensions," in *Proc. IEEE/RSJ Int. Conf. Intell. Robots Syst.*, San Francisco, CA, USA, Sep. 2011, pp. 2640–2645.

[46] J. Rosell *et al.*, "The Kautham project: A teaching and research tool for robot motion planning," in *Proc. IEEE Int. Conf. Emerg. Technol. Factory Autom.*, Barcelona, Spain, Sep. 2014, pp. 1–8.

[47] IOC-UPC. (Jul. 2017). *Human-Demonstrated Motion Planning for Anthropomorphic Dual-Arm Robots: Video of the Experiments*. [Online]. Available: https://sir.upc.edu/projects/human-demonstrated/index.html

Néstor García received the B.S. (Hons.) degree in industrial engineering from the Universitat Politècnica de Catalunya, Barcelona, Spain, in 2015, where he is currently pursuing the Ph.D. degree in automatic control, robotics and computer vision with the Institute of Industrial and Control Engineering.

His current research interests include task and motion planning, human–robot interaction, and multirobot cooperation and learning in robotic systems.

Jan Rosell received the B.S. degree in telecommunication engineering and the Ph.D. degree in advanced automation and robotics from the Universitat Politècnica de Catalunya (UPC), Barcelona, Spain, in 1989 and 1998, respectively.

He joined the Institute of Industrial and Control Engineering, UPC, in 1992, where he has developed research activities in robotics. He has been involved in teaching activities in automatic control and robotics with UPC, as an Assistant Professor since 1996, and an Associate Professor since 2001. His current research interests include task and motion planning, mobile manipulation, and robot co-workers.

Raúl Suárez (M'96) received the Electronic Engineer (Hons.) degree from the National University of San Juan, San Juan, Argentina, in 1984, and the Ph.D. (*cum laude*) degree from the Universitat Politècnica de Catalunya (UPC), Barcelona, Spain, in 1993.

He is a Research Supervisor with the Institute of Industrial and Control Engineering, UPC, where he was responsible for the research line on process control from 1998 to 2003, an Assistant Director from 2003 to 2009, the Director from 2009 to 2016, and has been the Coordinator of doctoral program on robotics since 1995. His current research interests include grasping and manipulation, mechanical hands, fixturing, assembly, task planning, telemanipulation, and manufacturing automation.